



Research Article

Unveiling nano-scale chemical inhomogeneity in surface oxide films formed on V- and N-containing martensite stainless steel by synchrotron X-ray photoelectron emission spectroscopy/microscopy and microscopic X-ray absorption spectroscopy



Xiaoqi Yue^a, Dihao Chen^{a,b}, Anantha Krishnan^c, Isac Lazar^d, Yuran Niu^e, Evangelos Golias^e, Carsten Wiemann^f, Andrei Gloskovskii^g, Christoph Schlueter^g, Arno Jeromin^g, Thomas F. Keller^{g,h}, Haijie Tongⁱ, Sebastian Ejnermark^c, Jinshan Pan^{a,*}

^a KTH Royal Institute of Technology, Division of Surface and Corrosion Science, Stockholm, 100 44 Sweden

^b University of Science & Technology Beijing, Institute of Advanced Materials & Technology, Beijing 100083 China

^c Uddeholms AB, Hagfors, 683 85 Sweden

^d Lund University, Division of Synchrotron Radiation Research, Lund, 221 00 Sweden

^e MAX IV Laboratory, Lund University, Lund, 221 00 Sweden

^f Peter Grünberg Institute (PGI-6), Research Center Jülich, Jülich, D-52425 Germany

^g Germany Centre for X-ray and Nano Science (CXNS), Deutsches Elektronen-Synchrotron DESY, Hamburg, 226 07, Germany

^h Department of Physics, Hamburg University, Hamburg, 201 48 Germany

ⁱ Institute of Surface Science, Helmholtz-Zentrum Hereon, Geesthacht, 215 02 Germany

ARTICLE INFO

Article history:

Received 13 February 2024

Revised 28 March 2024

Accepted 1 April 2024

Available online 21 April 2024

Keywords:

Synchrotron X-ray photoelectron emission microscopy

Hard X-ray photoelectron emission spectroscopy

Synchrotron microscopic X-ray absorption spectroscopy

Martensite stainless steel

Surface oxide film

ABSTRACT

Nano-scale chemical inhomogeneity in surface oxide films formed on a V- and N-containing martensite stainless steel and tempering heating induced changes are investigated by a combination of synchrotron-based hard X-ray Photoelectron emission spectroscopy (HAXPES) and microscopy (HAXPEEM) as well as microscopic X-ray absorption spectroscopy (μ -XAS) techniques. The results reveal the inhomogeneity in the oxide films on the micron-sized Cr₂N- and VN-type particles, while the inhomogeneity on the martensite matrix phase exists due to localised formation of nano-sized tempering nitride particles at 600 °C. The oxide film formed on Cr₂N-type particles is rich in Cr₂O₃ compared with that on the martensite matrix and VN-type particles. With the increase of tempering temperature, Cr₂O₃ formation is faster for the oxidation of Cr in the martensite matrix than the oxidation of Cr nitride-rich particles.

© 2024 Published by Elsevier Ltd on behalf of The editorial office of Journal of Materials Science & Technology.

This is an open access article under the CC BY license (<http://creativecommons.org/licenses/by/4.0/>)

1. Introduction

Martensitic stainless steels are used in of high performance components subjected to harsh environments. They have excellent mechanical properties and moderate corrosion resistance, and good wear resistance [1,2]. Their typical applications include plastic moulding, food processing, and marine applications, etc. [3]. The addition of alloying elements leads to blocking of slip planes and therefore improves the mechanical properties, and more importantly, the alloying can cause tremendous increase in the corrosion resistance if they contain sufficient Cr [4–6]. Due to its

high degree of reactivity, Cr is a major alloying element in stainless steels [7]. By forming an adherent, insoluble layer of reaction products on the surface, these alloys protect themselves from the chemical attack by corrosive agents [8]. For better corrosion resistance, Mo is also added in stainless steels in a range from 2 % to 4 % [9–12]. Even such small percentages of Mo have significant beneficial effects on the resistance of stainless steels to pitting and crevice corrosion in chloride environments [13,14]. Another alloying element, N, acts as an interstitial element and is known to show higher weight coefficient than the Cr and Mo in the formula of Pitting Resistance Equivalent number (PREN) [15]. Adding N has been found to increase the resistance to localised corrosion by the precipitation of Cr₂N instead of Cr₂₃C₆ particles in austenitic and duplex stainless steels with a low C content (< 0.03 wt.%) [16–18].

* Corresponding author.

E-mail address: jinshanp@kth.se (J. Pan).

It is necessary to add more N to substitute carbide for martensite stainless steel due to its higher C content [19,20]. The advantage is that nitride is believed to increase hardenability; however, the formation of Cr nitrides also consumes the Cr that is needed for forming protective oxide film on the surface. Thus, adding V to release Cr from nitrides is a good strategy since V has a strong tendency to form V nitrides [21,22]. These alloying elements work together to provide good mechanical properties, and the oxide film formed on the surface improves the corrosion resistance.

Chemical state of the surface layer (passive film and underlying metallic layer, nm in thickness) of advanced alloys determines the corrosion resistance [23,24], which is crucial for their applications. The passive film has a double-layered structure with the hydroxides as the outer layer and the oxides as the inner layer [25,26]. Furthermore, the composition of the metallic layer beneath the passive film has been found to differ from that of the bulk [22,27]. Under the passivation state, the passive film on stainless steels is normally regarded as a homogeneous layer, which is mainly a mixture of amorphous Cr and Fe oxides. However, it has been reported that some intermediate state of oxides may form on undissolved particles within the microstructure. The oxidation of nitrides or carbides show clearly a difference compared to the oxidation of metallic elements. Their oxides are thermodynamically stable under a higher potential range, especially for nitrides [22,28–30].

Tooling alloys often have complex microstructures consisting of different phases and grains with different orientations, and heat treatment may result in precipitation of micro- or nano-sized carbide and nitride particles in the microstructure [31,32]. It is expected that there are spatial variations in the chemical composition of the oxide film formed on different phases and grains. Usually X-ray photoelectron spectroscopy (XPS) is used for chemical analysis of the passive film [33]. However, to reveal the heterogeneity in the passive film remains a challenge in corrosion science. We have successfully utilized synchrotron hard X-ray photoelectron emission microscopy (HAXPEEM) to analyse the passive film on a super duplex stainless steel, the results revealed lateral variation of the passive film with a lateral resolution of 0.5 μm [34]. Advanced tooling alloys are increasingly used in industrial manufacture. The Cr content in the alloys enables a stainless property and heat treatments are used to achieve desirable mechanical strength, which, however, may lead to changes of the passive film. Recently, we have utilized ambient pressure XPS (APXPS) at the HIPPIE beamline at MAX IV, Sweden, to analyse natural and anodic passive films on a N- and V-containing tooling alloy [22]. The APXPS spectra show Cr and V nitrides in the surface layer and Fe, Cr, and V oxides in the passive film, but the results are averaged over the analysed area including both the matrix and particles.

Analysis of the passive film of V- and N-containing martensitic stainless steel with undissolved nitrides and evolution of hard phases with tempering at high temperatures is rare due to the complicated microstructure and the small dimensions of the par-

ticles. Detailed information about the lateral variation associated with the particles, and oxide film growth caused by the tempering are essential to understand the passivation behaviour and susceptibility to localised corrosion in severe environments. However, no literature can be found on V- and N-containing martensite stainless steel that provide such information. In this work, we focus on the investigation of the surface oxide film formed on the V- and N-containing martensite stainless steel with complex microstructure, and the evolution of the oxide film from ambient temperature to 600 °C. The chemical composition of the oxide film formed on the different phases is analysed by a combination of synchrotron-based Hard X-ray Photoelectron Spectroscopy (HAXPES) and Photoemission Electron Microscopy (HAXPEEM) at P22 beamline at PETRA III in DESY, Hamburg, Germany. Furthermore, the chemical evolution of the oxide film with the heating temperature is analysed by using microscopic X-ray absorption spectroscopy (μ -XAS) at MAXPEEM beamline of MAX IV, Lund, Sweden, with in-situ heating possibility.

2. Material and methods

2.1. Material and sample preparation

The sample material was a V- and N- containing martensite stainless steel, supplied by Uddeholms AB, Sweden, with the chemical composition (wt.%): C 0.36 %, Si 0.3 %, Mn 0.3 %, Cr 18.2 %, Mo 1.2 %, V 3.5 %, N 1.55 %, and Fe balance. The samples were cut in sizes of 10 mm \times 10 mm \times 3 mm, heated to austenitization temperature of 1080 °C for 0.5 h followed by quenching and tempering at 200 °C for 2 times (ex-situ heat treatments). The effect of microstructure on the passive film characteristics was investigated by comparing the composition of the surface layer after different in-situ heating procedures. Furthermore, parallel samples austenitized at 1010 °C were also measured to investigate the effect of austenitization temperature. The detailed heat treatment processes and subsequent surface analyses are provided in Fig. 1.

The analysed surface of the samples was ground down to 1-micron diamond suspension (Struers, Denmark). Then, the sample surface was carefully cleaned with acetone, ethanol, and deionised water, and then dried by air blow. Prior to the experiments, the sample was storage in ethanol to avoid oxidation in air.

2.2. HAXPEEM and HAXPES measurements

The HAXPEEM measurement was performed at DESY (Deutsches Electron Synchrotron) to extract surface chemical information from different phases in the martensite stainless steel. The microstructure of the sample was characterized by Scanning Electron Microscope (SEM) using a FEI Nova NanoSEM instrument with Back-scattered Electron Detector [35]. The region of interest (ROI) was marked with 3 Pt fiducial deposits of decreasing size, as shown in Supplementary Fig. 1. The ROI around the smallest

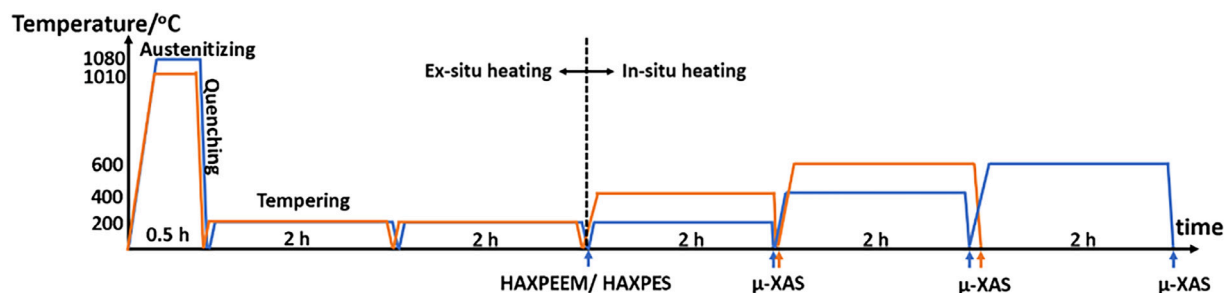


Fig. 1. Ex-situ and in-situ heat treatment processes of the V- and N- containing martensite stainless steel before and during the surface analysis experiments.

square Pt mark is shown in the SEM image in Fig. 2, where the square Pt deposit was positioned at the right bottom corner of the image. Following this procedure, the sample was transferred to ultrahigh vacuum (UHV 10^{-9} mbar) at the P22 beamline at PETRA III at DESY for the HAXPEEM measurement by utilizing an imaging energy filter (NanoESCA, Focus GmbH) that was operated in collaboration with Forschungszentrum Jülich. The Pt markers can be observed easily in PEEM mode under UV light excitation where they show high contrast due to the difference in work function from that of the Fe based matrix. More detailed information of the Pt markers has been described in previous work [34].

The HAXPEEM measurement was performed at 4 keV photon energy with a lateral resolution of $0.5\ \mu\text{m}$ [34]. In XPS mode, spectra over a narrow energy range of Fe $2p_{3/2}$, Cr $2p_{3/2}$, V $2p_{3/2}$, and N $1s$ were measured consecutively, with an energy resolution of 1 eV and 60 ksec dwelling time. The spectrum of Pt $3d_{5/2}$ was also measured for internal calibration of the energy shift due to electrostatic charge on the sample surface. Then, the sample was taken out from the HAXPEEM chamber, transferred to the HAXPES chamber [36], and measured at 6 keV with a step width of 0.05 eV and high energy resolution of 0.23 eV for a large surface area including the ROI. The probing depth was determined by the inelastic mean free path (IMFP, i.e., λ) of the electrons in the material, with 3λ corresponding to the depth above which $\sim 95\%$ of the signal originates.

Analysis of the XPS spectra was performed after summing up signals originated over the different phases in the microstructure to gain a sufficient intensity-to-background ratio. Hence, signal intensities of individual core levels show contrasts in the surface area that can be compared with the different phases in the microstructure seen in the SEM image. The XPS peak identification and spectra fitting were made based on the high-resolution HAXPES results, which were used to assist quantitation the HAXPEEM signals originated from different regions.

2.3. μ -XAS measurement

The μ -XAS measurement was performed at MAX IV laboratory (Swedish national laboratory) to investigate the surface chemical composition of the different phases in the microstructure and the evolution with the temperature increase [37]. Prior to the synchrotron measurement, the sample was mounted into the sample holder with a Mo cap, and then introduced into the preparation chamber for pre-vacuum to around 10^{-10} mbar. By using a transfer arm, the sample was transferred to the analysis chamber ($\sim 10^{-11}$ mbar) which hosts the aberration-corrected Spectroscopic Photo-Electron and SPELEEM microscope (Elmitec GmbH). In XAS mode, spectroscopic images of the Fe L-edge, Cr L-edge, V L-edge & O K-edge, and N K-edge were collected, with an energy resolution of 0.2 eV.

The sample was heated from ambient temperature to 400 °C by radiative heating with a filament built in the sample holder, and further heated up to 600 °C by e-beam bombardment. The temperature of the sample was recorded in real time by a type-C thermocouple spot-welded on the Mo ring under the sample, which was also checked by using an infrared pyrometer. All heating steps lasted 2 h after reaching the target temperature, followed by the cooling by cold nitrogen gas at 85 K, which was slower than under ambient pressure condition due to a low heat conduction in UHV condition.

Analysis of the image files collected at MAXPEEM beamline was performed in ImageJ (Fiji) [38]. Each absorption image stack was aligned using the TurboReg plugin [39] accounting for any sample drift during measurements. Each image stack was then normalised by an image recorded in the pre-edge region, to exclude any work function contrast. Note that the V L-edge and O K-edge

image stack was normalised by an V pre-edge. μ -XAS spectra from selected regions of interest (corresponding different phases) were then exported from the aligned and normalised image stack.

3. Results

Fig. 2 shows the HAXPEEM maps for various core levels on the V- and N- containing martensite stainless steel after austenitization at 1080 °C, with the energy step of 1 eV. The intensity for different areas is calibrated based on the background signal at 572, 511, 705, and 395 eV for Cr $2p_{3/2}$, V $2p_{3/2}$, Fe $2p_{3/2}$, and N $1s$, respectively. The intensity map of Cr $2p_{3/2}$ presents the highest intensity at binding energy of 574 eV. Micron-sized regions marked by red dotted lines show higher signal intensity than surrounding areas, especially at 574 eV, which correspond the CrN-domains according to the SEM images. The large light-grey particles are Cr nitrides, whereas the small dark-grey particles are V nitrides (Supplementary Fig. 2). In the maps of V $2p_{3/2}$, the signal for the martensitic matrix is relatively low because of the low content of V in the stainless steel. Instead, V is enriched in some regions marked by dotted blue lines, showing the highest signal intensity at 513 eV, which correspond the VN-domains according to the SEM images. Note that the Cr and V enriched areas are not correlated, but they partially overlap. The corresponding maps of Fe $2p_{3/2}$ and N $1s$ with the marked areas are also included in Fig. 2 for comparison. In the maps of Fe, the matrix area show intense signals as Fe is the base element for this stainless steel. In contrast, the Cr and V enriched regions show a lower content of Fe, especially at 706 and 707 eV. For the N $1s$ maps, the total signal is minor but a higher intensity can be seen from the Cr and V enriched regions at 397 eV. The corresponding SEM image of the focused area indicates that the Cr and V enriched regions mainly include second particles, which are Cr and V nitrides.

Fig. 3 presents the high energy-resolution HAXPES results collected from the whole surface and the normalized intensity of the HAXPEEM results from the unit area of the centre of Cr nitride and V nitride domains ($0.5\ \mu\text{m} \times 0.5\ \mu\text{m}$). By combining both of the results, one can achieve a high spatial resolution while making up for the lack of energy resolution of HAXPEEM. Note that the use of a large energy step for HAXPEEM measurements is necessary to collect enough data showing the spatial resolution within small areas. Whereas, the HAXPES measurement was performed on a large area with a small energy step of 0.05 eV, giving a high energy resolution of the XPS spectra. For the HAXPES and HAXPEEM measurements, the photon energies used are 6000 and 4000 eV, respectively, so that probing depths are approximately 19 and 11 nm, respectively, ca. five or more times of the passive film thickness. This implies that several times thicker matrix/second phases than the surface oxide layer are probed, giving the signal intensities of both passive film and underlying metallic layer in the XPS spectra.

As shown in the Cr $2p_{3/2}$ spectra (Fig. 3(a)), the highest intensity at 574 eV corresponds to the metallic Cr. The highest signal intensity of Cr oxide and hydroxide is observed on the surface of the Cr nitride domains, followed by the martensite matrix, and the lowest on the V nitride domains. In contrast, high signal intensities of metallic V and V oxides are seen on the surface of the V nitride domains (Fig. 3(b)), while the V signals are weak on the Cr nitride domains and negligible on the martensite matrix. As expected, the spectra of Fe $2p_{3/2}$ in Fig. 3(c) show that the signal intensities of metallic Fe and Fe oxides in the Cr nitride and V nitride domains are lower than that of the martensite matrix. The results of N $1s$ in Fig. 3(d) indicate that the N in this stainless steel mainly forms second phase particles, while its content in the matrix is negligible. The results of O $1s$ spectrum obtained by HAXPES confirm the presence of oxides and hydroxides, as shown in Supplementary Fig. 3.

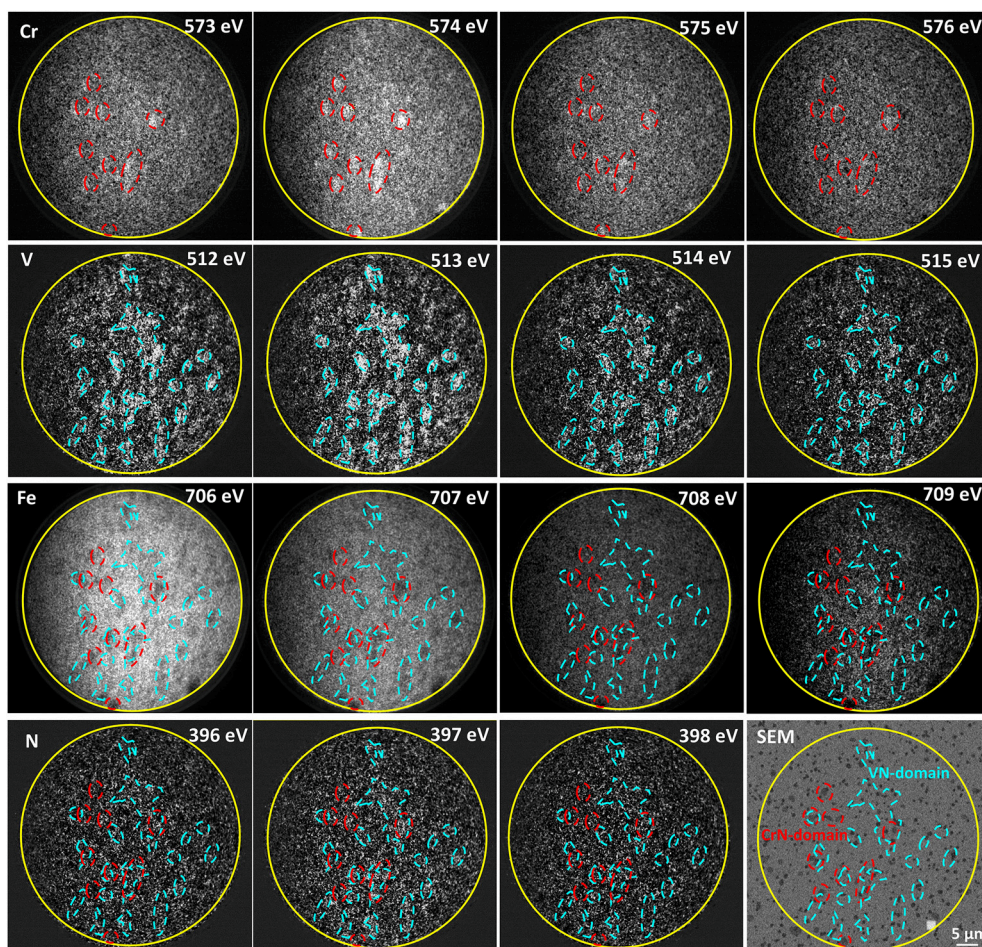


Fig. 2. HAXPEEM maps for Cr 2p, V 2p, Fe 2p, and V 1s at specific binding energies obtained on the ROI of V- and N-containing martensite stainless steel. The same ROI is shown in the backscattering SEM image. The sample was austenitized at 1080 °C and tempered at 200 °C.

The HAXPEEM results reveal that the oxide film composition is different on the surface of the martensite matrix, the Cr nitride domains, and V nitride domains. Fig. 4 shows the HAXPEEM mapping at 577 and 710 eV, corresponding to Cr- and Fe-oxides, respectively, which are the main components of the passive films on stainless steels [26,40,41]. Although the signal intensity is relatively low due to the nano-scaled areas, the difference in the intensity between the matrix and second phase particles is significant, showing less Fe oxides on the second phases, but more Cr oxides on the Cr nitride particles. The binding energies of different core levels are usually well separated, however, the chemical shifts between metal nitrides and oxides (M–N and M–O bonds) are relatively small and show overlap. Therefore, the photoelectrons escaped from the surface could originate by multiple compounds, so the HAXPEEM with a low energy-resolution is not sufficient to ascertain the chemical composition variation in the surface film related to the microstructure, and the combination with the HAXPES with a high energy-resolution is necessary.

The μ -XAS measurements provided further information of the chemical inhomogeneity in the surface oxide films on the V- and N-containing martensite stainless steel, and the heating possibility at the instrument enabled in-situ monitoring of the evolution of surface film with the increasing temperature. Note that the information of oxides, hydroxides, and metal are all included in the data. However, the amount of the hydroxides is negligible compared with that of the oxides. Furthermore, hydroxides tend to transform to oxides via dehydration under UHV and heating conditions [22,42]. Therefore, only oxides are considered in the dis-

cussion of the μ -XAS results. The sequences of images of absorbing photon intensity were recorded with the energy step of 0.2 eV. The interpretation and modelling of the XANES spectra is complicated, and it is therefore used as a fingerprinting technique, which is able to evaluate the evolution of electronic structure of specific surface area, which depends on the chemical environment and bonding geometry.

Fig. 5 shows μ -XAS images obtained at photon energy of 708.8 eV and different temperatures, as well as the Fe L-edge XANES spectra extracted from the martensite matrix (Green), V nitride-rich region (Orange), and Cr nitride-rich region (Grey), respectively, as marked in the images. The μ -XAS images in the right column are normalized based on the intensity distribution at the pre-edge (the same applies to data processing for other absorption edges). Therefore, the image contrast shows the spatial distribution of a specific absorption edge feature at the selected energy, which is in turn related to a specific chemical species. Note that these images present the absorbing intensity at 708.8 eV (line A), which corresponds to the energy with highest intensity in the Fe L-edge XANES spectra. The total μ -XAS image sequence with the function of photon energy is shown in the Supplementary video 1. The XANES spectra in the left column are extracted based on the normalized μ -XAS image sequence, and have been further normalized to the unit area of the chosen circles.

The shape of the Fe L-edge spectra shows evidence of Fe^0 character in the martensite matrix. At ambient temperature, the metallic component labelled by A is accompanied by a small shoulder at higher energies in the region labelled by B. This higher en-

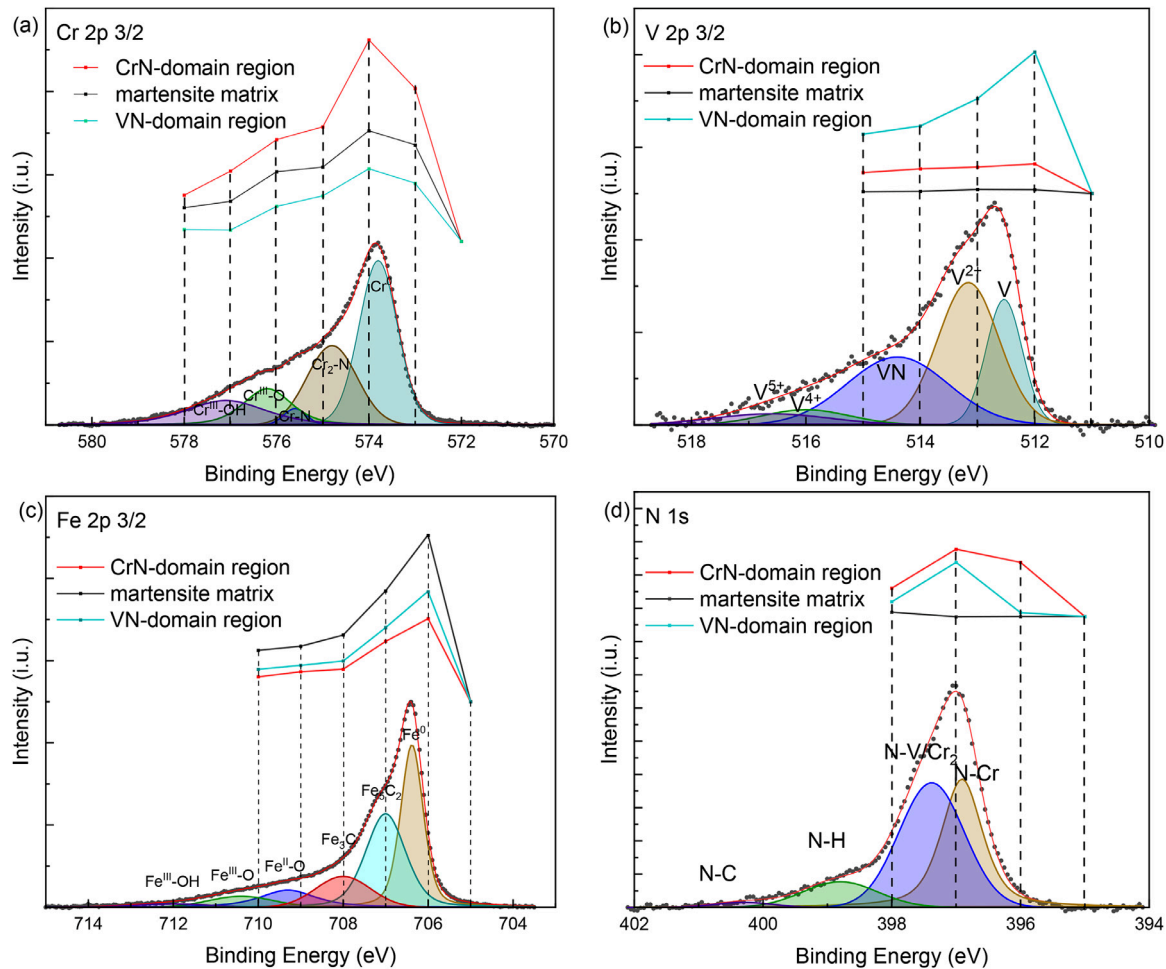


Fig. 3. XPS spectra of the peak 2p_{3/2} for (a) Cr, (b) V and (c) Fe and 1s for (d) N obtained by HAXPEEM from the central area of the Cr nitride and V nitride domains (0.5 μm \times 0.5 μm). These spectra are compared with the high-resolution XPS spectra from the HAXPES for the whole ROI to assist the peak identification.

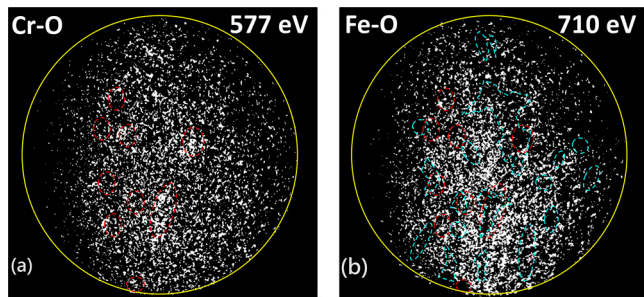


Fig. 4. HAXPEEM mapping for (a) Cr 2p at 577 eV and (b) Fe 2p at 710 eV on the ROI of the V- and N-containing martensite stainless steel.

ergy shoulder corresponds to features associated with oxidised Fe [43,44]. The metallic character of the Fe L-edge originates from the alloy beneath the oxide film, indicating that the probing depth of several nanometres is deeper than the passive film. The detailed discussion of the oxide film will be given in the following parts of the Cr L-edge and O K-edge results. The Fe spectra of the martensite matrix can be directly compared to that of the secondary phase displayed in orange colour. The overall absorption intensity of the secondary phase is much smaller than that from the martensite matrix, because the main component of the secondary phase (mainly Cr and V nitrides) is not related to a Fe compound. The two broad peaks separated by 13 eV are assigned to L3 (Fe

2p_{3/2}-3d) and L2 (Fe 2p_{1/2}-3d) transitions, owing to the spin-orbit coupling. The total intensity at the Fe L-edge reflects the absorption intensity of Fe⁰ from the matrix, and it gradually decreases as the temperature increases from ambient temperature to 600 °C. This phenomenon can be caused by the thickening of the surface film which impedes the escape of electrons. The decrease in overall intensity, coupled with no obvious peak of Fe^{II} and Fe^{III} from the Fe L-edge spectra indicate that the growth of the oxide film with elevated temperature is not primarily dependent on Fe oxidation. Moreover, the shoulder at region B of the Fe L-edge is even disappeared after heating at 200–600 °C, which indicates the loss of O from the native oxidized Fe. The missing O can be either taken up by the other alloying elements (Cr or V) or evaporate into the vacuum.

Fig. 6 presents μ -XAS images obtained at photon energy of 578.2 eV and different temperatures, as well as the Cr L-edge XANES spectra extracted from the martensite matrix (Green), V nitride-rich region (Orange), and Cr nitride-rich region (Grey), respectively, as marked in the images. The Cr L-edge spectra correspond to the transitions from a ground-state 2p⁶3d³ to one of the final-states 2p⁵3d⁴. On the martensite matrix, the features A and B in the spectra resemble those of the published data of Cr^{III} valence state in Cr₂O₃ [45], while the spectra from the secondary phases show similar features to those of grown Cr nitride films [46]. At ambient temperature, the most intense signal comes from Cr nitrides in the Cr nitride-rich region, followed by the Cr oxide signal detected on the martensite matrix, and then Cr nitrides in

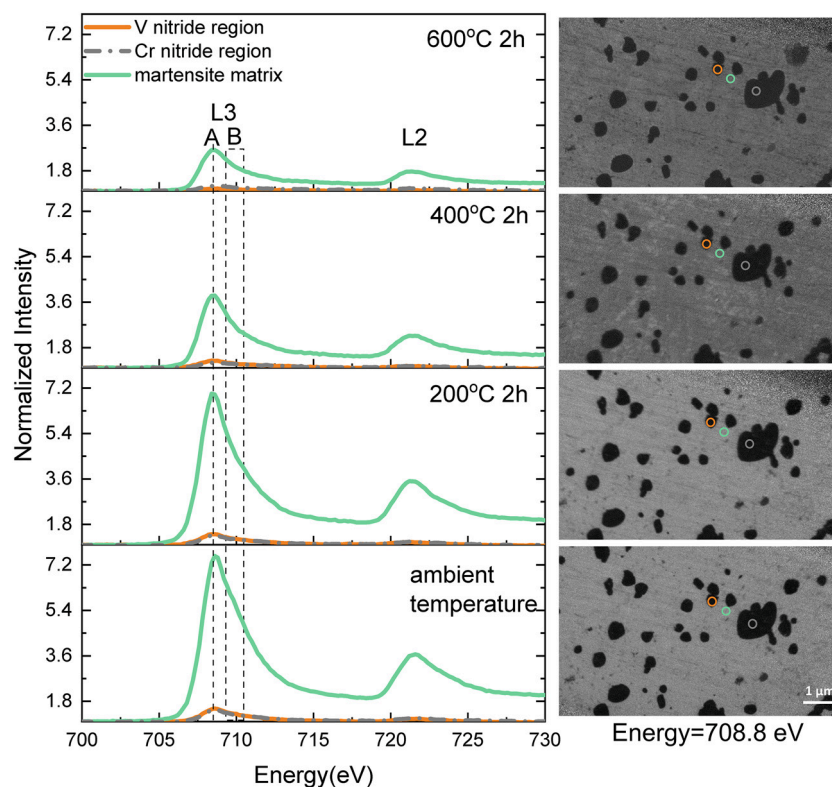


Fig. 5. μ -XAS images at photon energy of 708.8 eV and corresponding Fe L-edge XANES spectra extracted from the martensite matrix (Green), V nitride-rich region (Orange), and Cr nitride-rich region (Grey), respectively, of the V- and N-containing martensite stainless steel at ambient temperature, 200, 400 and 600 °C. The colour circles on the images are marked regions from which the spectra are extracted. The sample was austenitized at 1080 °C.

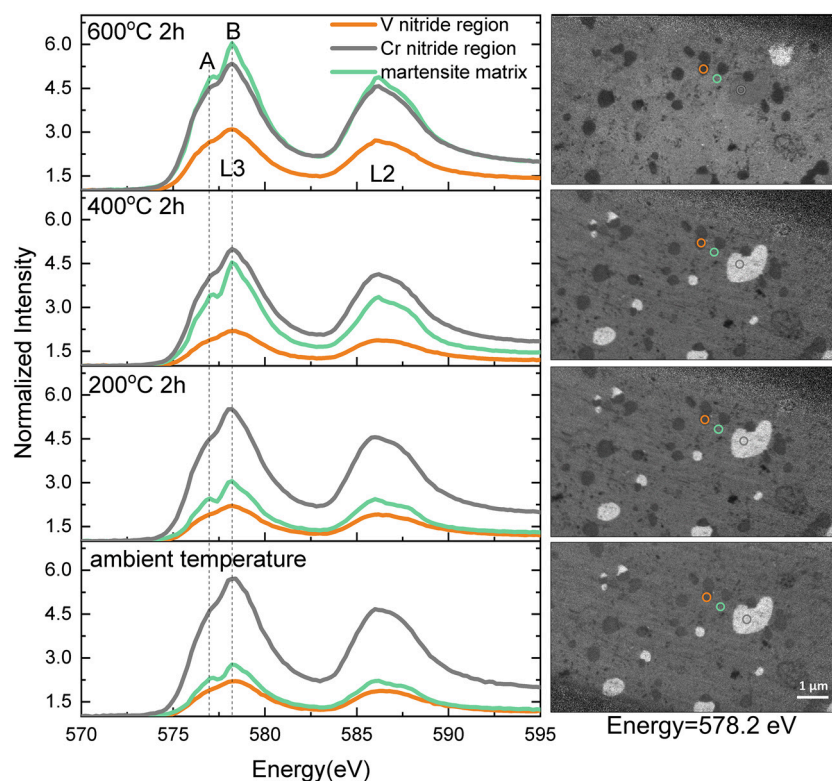


Fig. 6. μ -XAS images at photon energy of 578.2 eV and corresponding Cr L-edge XANES spectra extracted from the martensite matrix (Green), V nitride-rich region (Orange), and Cr nitride-rich region (Grey), respectively, of the V- and N-containing martensite stainless steel at ambient temperature, 200, 400 and 600 °C. The colour circles on the images are marked regions from which the spectra are extracted. The sample was austenitized at 1080 °C.

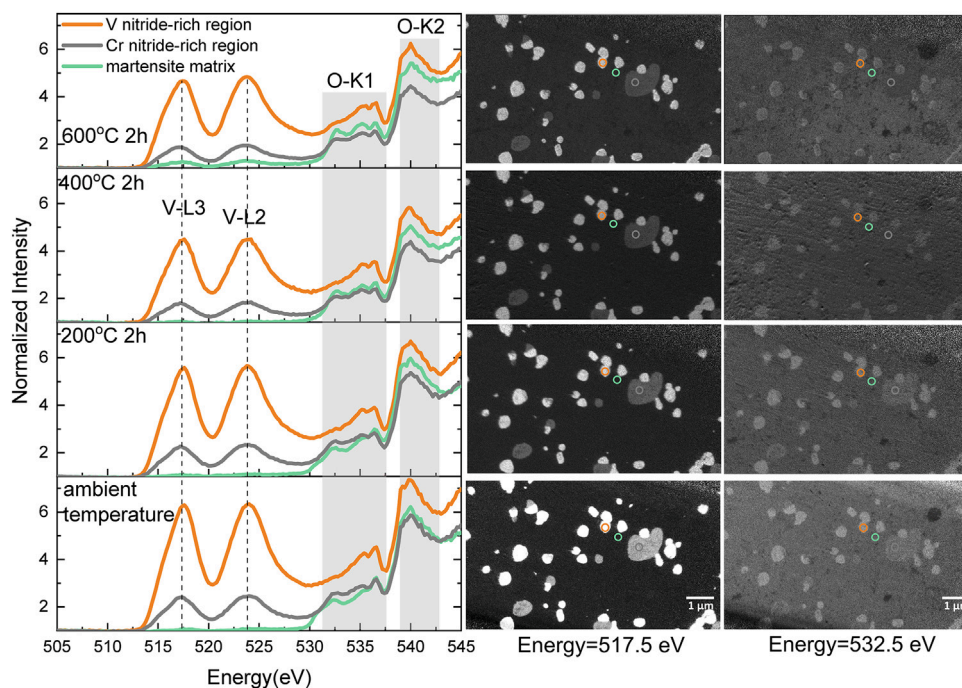


Fig. 7. Comparison of the XANES spectra of V L-edges and O K-edge, and corresponding μ -XAS images at photon energy of 517.5 and 532.5 eV obtained at ambient temperature and after in-situ heating up to 600 °C on the V- and N-containing martensitic stainless steel. The colour circles on the images are marked regions from which the spectra are extracted. The sample was austenitized at 1080 °C.

the V nitride-rich region. It is noted that the intensity of Cr_2O_3 on the martensite matrix gradually increases with the rise of temperature, which corresponds to the thickening of a surface film composed of Cr_2O_3 . In comparison, the changes in the intensity on the secondary phase is less affected by the heating, however, the feature A becomes more pronounced, suggesting an increase of Cr_2O_3 component. The corresponding μ -XAS images at 578.2 eV show a high intensity at the Cr nitride-rich region from ambient temperature to 400 °C. However, the intensity difference between the martensite matrix and the Cr nitride-rich region is reversed as the temperature increases to 600 °C, showing higher intensity of Cr^{III} compounds at the matrix region than the Cr nitride-rich region. The evolution with the increasing temperature suggests that the growth of surface layer composed of Cr_2O_3 occurs preferentially on the martensite matrix. Although the oxidation of nitrides is also promoted as the temperature increases, the nitride to oxide transformation is relatively slow.

Similar to above interpretation of the results, Fig. 7 shows the μ -XAS images and corresponding XANES spectra of V L-edge and O K-edge. Highest intensity of VN is observed at photon energy of 517.5 eV on the V nitride-rich region, followed by the Cr nitride-rich region; and this confirms the mixed structure of the secondary phase. Whereas, the intensity of V L-edge is negligible on the martensite matrix at ambient temperature. Furthermore, the V L2-edge trails to the O K-edge. Due to O species in the beamline optical elements, absorption occurs upstream, leading to a drop in incoming beam intensity at energies above 535 eV, which subsequently normalize intensity based on the photon flux (as a function of photon energies), while the photon flux is calculated by the photodiode current and the quantum efficiency of the photodiode (again a function of photon energies). The peaks around 532 eV originates from the metal ions' d orbitals that are hybridized with O 2p orbitals, marked as K1. This evidently shows there are O atoms chemically bound to the alloy (at the surface). A broad main peak is observed in the 540 eV range from unoccupied sp states in O 2p-metal, which is marked as K2. Nevertheless, the combined

appearance of the V L-edge and the initial part of the O K-edge that is visible on V nitride-rich region resembles the electron yield spectral features of oxynitride [47]. In contrast, the O K-edge on the matrix and Cr nitride-rich region show peak features around 532.5 eV that are consistent with oxides on the sample surface [48,49].

With the increase of temperature, the intensities of V L-edge decrease on both V nitride and Cr nitride-rich regions, but increase on the martensite matrix. The O K-edge increases in intensity on the martensite matrix region, in agreement with the increase of Cr_2O_3 (film) intensity and the decrease of Fe (matrix) intensity. In comparison, the O K-edge features stemming from oxides on the Cr nitride-rich region are not noticeably altered by the increasing temperature, which is confirmed by the Cr L-edge as well. On the other hand, the O K-edge increases in intensity (small bump at 532.5 eV) on the V nitride-rich region after the whole heating process.

Overall, the results in Fig. 7 suggest that the heating process facilitates the formation of V^{III} compounds in the martensitic matrix. The higher temperature promotes the oxidation reactions more on the martensite matrix compared with the Cr- and V-nitrides; and the thickening of the surface film is dominated by the growth of Cr_2O_3 .

A comparison of the XANES spectra of the N K-edge features on various phases at different temperatures is shown in Fig. 8, together with the μ -XAS images at 398.7 eV. The N K-edge shows four prominent features at 398.7, 400.4, 406.9 and 411.2 eV, labelled as K1, K2, K3, and K4, respectively. Here features K1 and K2 correspond to electronic transitions to the unoccupied hybridized states of N 2p and metal 3d orbitals, while features K3 and K4 are assigned to the unoccupied N 2p states hybridized to metal 4sp orbitals [50]. However, it should be noted that the intensities K3 and K4 show minor features on the Cr nitride-rich region compared with the V nitride-rich region, indicating that in the former case N is mainly in the hexagonal Cr_2N phase rather than the cubic CrN phase [51]. With the increase of temperature, the intensities of N

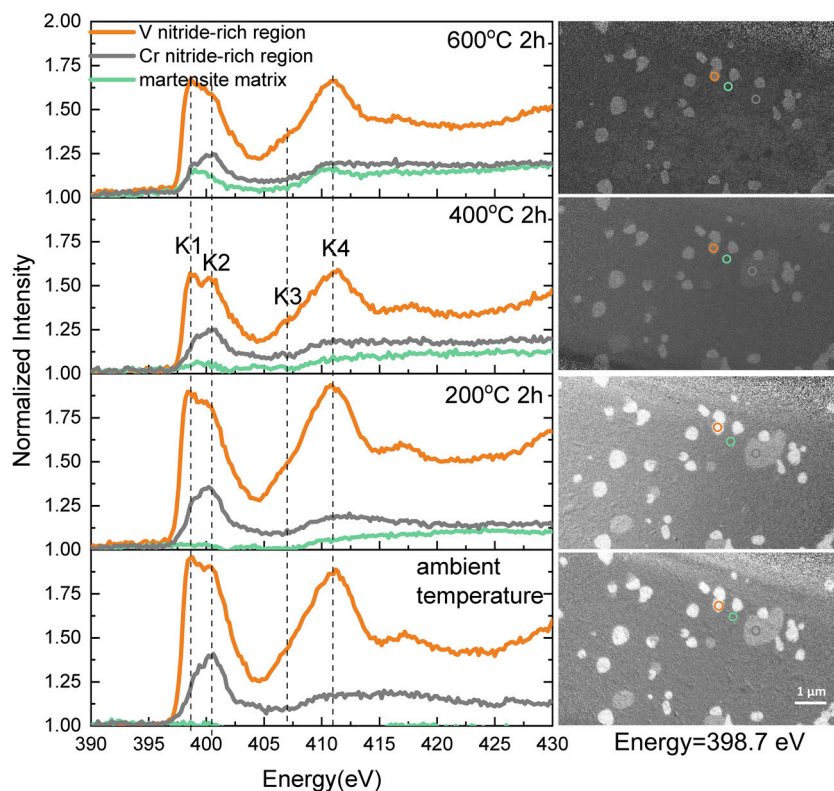


Fig. 8. Comparison of the XANES spectra of N K-edges and corresponding μ -XAS images at photon energy of 398.7 eV obtained at ambient temperature and after in-situ heating up to 600 °C on the V- and N-containing martensitic stainless steel. The colour circles on the images are marked regions from which the spectra are extracted. The sample was austenitized at 1080 °C.

K-edge on both the Cr- and V-nitride-rich region decrease, indicating the formation of oxides covering on the surface. The N K-edge features emerge on the martensite matrix region after heating at 600 °C, consistent with the observation of V^{III} compounds in the martensite matrix as mentioned above, which indicates the formation of tempering nitrides in the martensite matrix.

4. Discussion

Overall, the results show that all the phases are able to oxidize and form a surface oxide film on the N- and V-containing martensitic stainless steel. The microscopic analyses revealed inhomogeneities in the oxide film, i.e., there are differences in the composition of the oxide film formed on the martensitic matrix and the secondary phases. The martensite matrix shows a preferential formation of Cr_2O_3 , which is the key product to improve the corrosion protection compared to the Fe oxides formed on the base metal (Fe). According to the results from the HAXPEEM/HAXPES and μ -XAS measurements, more Cr_2O_3 is formed on the surface of Cr nitrides (mostly Cr_2N) at ambient temperature, indicating that the formation of Cr_2O_3 can occur via the oxidation of Cr_2N . However, this oxide formation is less promoted by the temperature increase compared with the oxidation of metallic Cr in the martensite matrix. On the surface of V nitrides (VN domain), in addition to V oxides, Cr_2O_3 is also detected, which could be formed by oxidation of small amount of Cr nitrides in the nitride mixture. Anyway, the Cr_2O_3 content is low in oxide film on the surface of V nitride domains at ambient temperature, and the growth of Cr_2O_3 is minimal with increasing temperature due to relatively slow nitride oxidation reaction. The results indicate that the Cr_2N particles (secondary phase) form native oxide film with the highest content of Cr_2O_3 , the martensite matrix phase forms the mixed oxides of Fe and Cr with a lower content of Cr_2O_3 , and the V nitrides

(secondary phase) form V oxides with a minor amount of Cr_2O_3 . With increasing temperature, the oxide growth rate is higher on the martensite phase compared with the secondary phase particles.

The in-situ μ -XAS measurements shown in Figs. 7 and 8 suggest that tempering VN formed within the martensite matrix phase after heating at 600 °C, which leads to an increased complexity of the microstructure. This implies that even the oxide film on the martensite phase may vary in the composition, especially for cases where the Cr content is insufficient, because the formation of secondary particles and tempering particles in the martensitic matrix may lead to local depletion of Cr in the vicinity of the particles.

In a previous study, we have observed that the Cr content in the martensite phase of this N- and V-containing stainless steel is influenced by the austenitization temperature (1010 °C vs. 1080 °C), which strongly affects the formation and stability of the passive film, as well as electrochemical properties and corrosion resistance of this martensitic stainless steel [22]. The Cr content in the metallic layer and Cr_2O_3 content in the oxide layer is relatively lower due to relatively insufficient dissolution of Cr nitrides into martensite matrix during the austenitization process at lower temperature. In order to investigate the passive film features with insufficient Cr, the XANES features for the samples with lower austenitization temperature (1010 °C) are analysed to gain further information about the oxide formation process relevant for tempering. Fig. 9 shows the intensity variations of Cr L-edge and their evolution with the in-situ heating temperature. Although the heating to 400 and 600 °C also leads to the oxidation of Cr and the thickening of the surface oxide film, the signal intensity of Cr_2O_3 on the martensite matrix does not exceed that of the Cr_2N region for the sample austenitized at 1010 °C. Additionally, the martensite matrix shows varying intensity in the images after tempering at 600 °C (top image in Fig. 9). As mentioned earlier, the brightness differ-

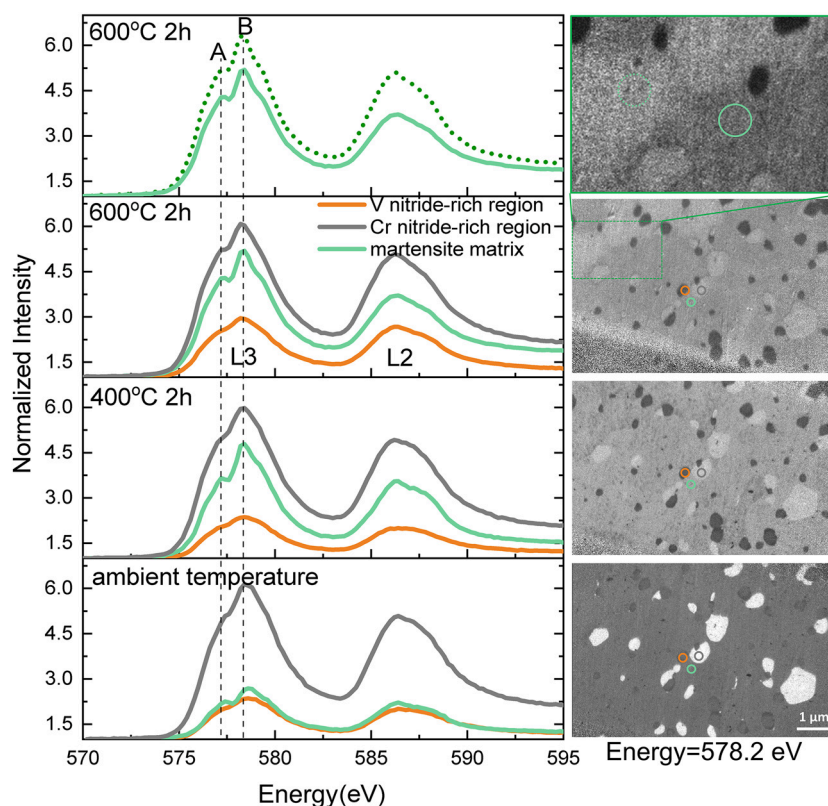


Fig. 9. Comparison of the XANES spectra of Cr L-edge and corresponding μ -XAS images at photon energy of 578.2 eV obtained at ambient temperature and after in-situ heating up to 600 °C on the V- and N-containing martensitic stainless steel. The sample was austenitized at 1010 °C (insufficient solution treatment). The colour circles on the images are marked regions from which the spectra are extracted.

ence represents the difference in the Cr content. The dotted circle area shows higher intensity compared with the solid circle area, indicating a more enrichment of Cr in this area and leading to inhomogeneity of the oxide film even within the martensite matrix phase. The inhomogeneity is also clearly shown in the Supplementary video 2.

Fig. 10 displays the Fe K-edge features and μ -XAS images of the martensitic stainless steel austenitized at 1010 °C, showing the effect of the heating up to 600 °C. A decrease of signal intensity of Fe K-edge is seen as the temperature increases from ambient temperature to 600 °C, which is likely due to the growth of a Cr_2O_3 -rich oxide that attenuates the Fe signal from the underneath metal. The comparison of the spectral intensity from the set of μ -XAS measurements reveals that the composition of the oxide film and the underlying metallic layer is different for the selected areas within the martensite matrix, e.g., the dotted circle area contains higher amount of Cr_2O_3 and Cr in the oxide film and the underlying metallic layer compared with the solid circle area. The oxide layer is thicker with more Cr_2O_3 in the dotted circle; while the Fe signal, which is mostly from the metal underneath, gets attenuated.

The XANES spectra of V L-edge and O K-edge and corresponding μ -XAS images of V^{III} at 517.5 eV and metal oxides at 532.5 eV provide further information on the martensitic stainless steel austenitized at 1010 °C, as shown in Fig. 11. The thickening of surface oxides on all phases, as well as the formation of tempering nitrides within the martensite matrix are observed as the temperature increases, which are very similar to the behaviours occurred on the 1080 °C austenitized samples. The evolution of the spectra of O K-edge of the martensite matrix phase of 1010 °C austenitized sample are identical to the results of the Cr L-edge, which shows an increase in the signal intensity with increasing temperature, but it does not exceed that on Cr_2N region after heating at 600 °C. Com-

paring with the μ -XAS images at the Cr and Fe L-edge, there is only minor variation in the V L-edge and O K-edge intensity in the martensite matrix. This is due to the fact that the amount of V in the martensite matrix is negligible compared with the secondary phase, whereas the O K-edge spectra indicate that the amount of the oxide film is quite uniform on the martensitic matrix.

As shown in Fig. 12, the XANES spectra of N K-edge of the 1010 °C austenitized martensitic stainless steel are characterized by the asymmetric features of Cr nitrides and V nitrides, showing the highest intensity at 398.7 and 400.4 eV, respectively. The formation of tempering nitrides during the in-situ heating is also observed in the martensite matrix when the temperature reached to 600 °C. It is noted that the peak position of the N K-edge spectra is different on the dotted circle area and solid circle area, which appears at the peak for Cr nitride and V nitride, respectively. This indicates that in the dotted circle area, V preferentially combines with N to form VN type nitrides in the martensite matrix during the heating process; therefore, more Cr is available to form oxides upon oxidation. However, in the solid circle area, more Cr is occupied by forming tempering nitrides, resulting in less Cr oxides composed in the oxide film formed at lower temperatures. This also leads to inhomogeneity in the surface oxide film on the martensitic stainless steel austenitized at 1010 °C. In all, the pronounced inhomogeneity and relatively lower Cr content in the surface oxide film may explain a lower corrosion resistance of the martensitic stainless steel austenitized at 1010 °C as observed previously [22].

Based on the combined results from this study, the diagram in Fig. 13 schematically illustrates the nano-scaled chemical inhomogeneity of the native oxide film formed on the different phases of the V- and N-containing martensitic stainless steel, as well as their evolution with the heating temperature relevant for tempering. The Cr_2N and VN regions form an oxide film composed mainly

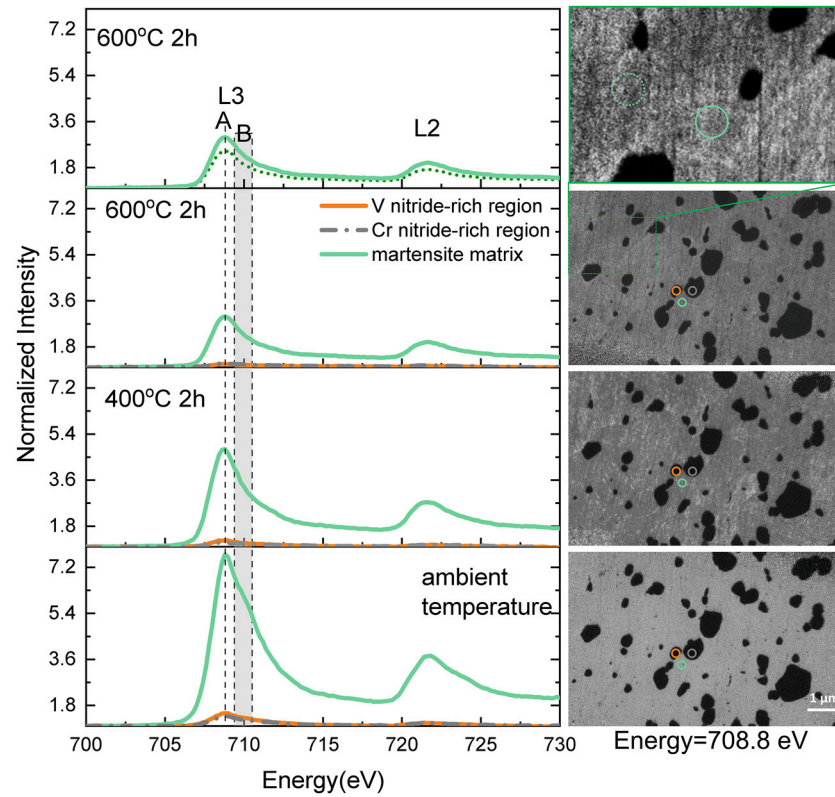


Fig. 10. Comparison of the XANES spectra of Fe L-edge and corresponding μ -XAS images at photon energy of 708.8 eV obtained at ambient temperature and after in-situ heating up to 600 °C on the V- and N-containing martensite stainless steel. The sample was austenitized at 1010 °C. The colour circles on the images are marked regions from which the spectra are extracted.

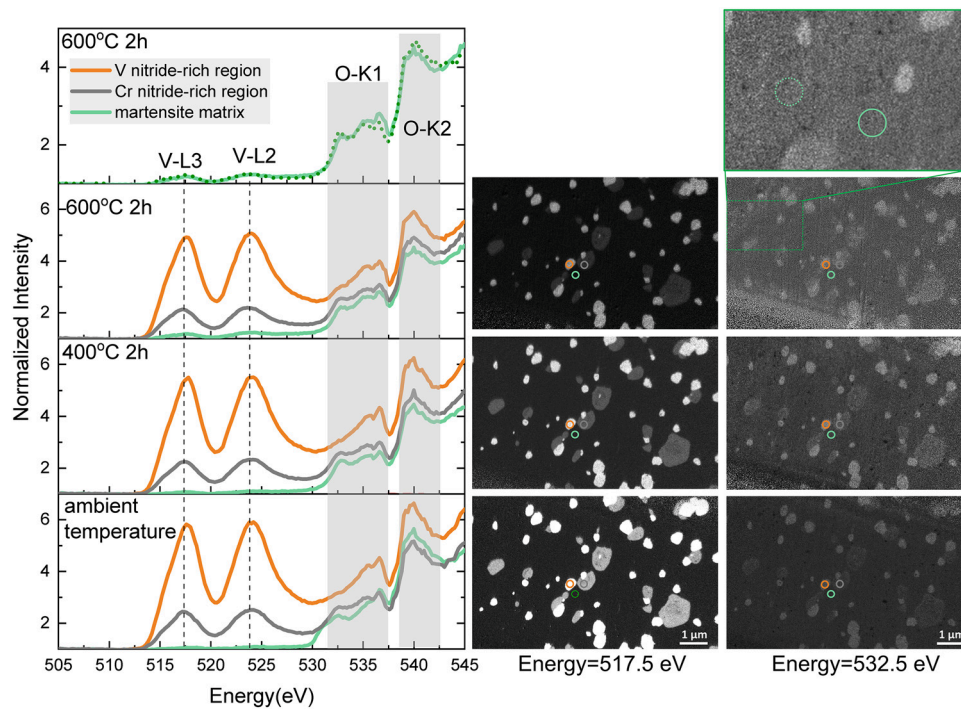


Fig. 11. Comparison of XANES spectra of V L-edges and O K-edge, and corresponding μ -XAS images at 517.5 and 532.5 eV obtained at ambient temperature and after in-situ heating up to 600 °C on the V- and N-containing martensite stainless steel. The sample was austenitized at 1010 °C. The colour circles on the images are marked regions from which the spectra are extracted.

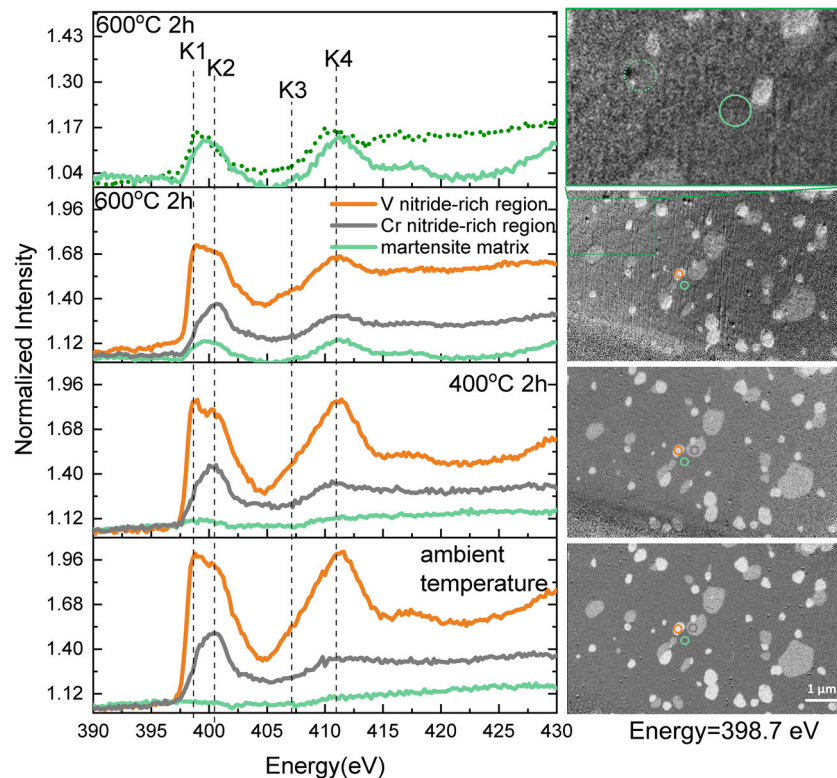


Fig. 12. Comparison of XANES spectra of N K-edges and corresponding μ -XAS images at 398.7 eV obtained at ambient temperature and after in-situ heating up to 600 °C on the V- and N-containing martensite stainless steel. The sample was austenitized at 1010 °C. The colour circles on the images are marked regions from which the spectra are extracted.

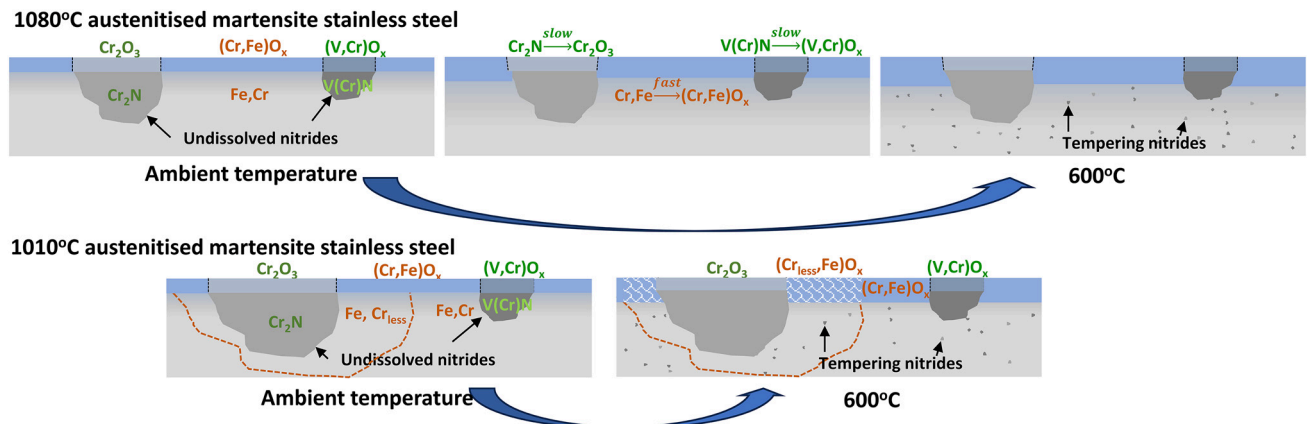


Fig. 13. Schematic diagram illustrating the nano-scaled chemical inhomogeneity passive film formed on V- and N-containing martensite stainless steel and the evolution with increased tempering temperature. Upper part: austenitized at 1080 °C, and down part: austenitized at 1010 °C.

of Cr oxide and V oxides, with a minor amount of Fe oxides compared to the oxide film formed on the martensite phase. The heating up to 600 °C promotes the oxide growth, and the thickness of oxide film on the martensite phase increases significantly. In contrast, the oxidation of the nitrides is much slower even at 600 °C. The formation of tempering nitrides (mainly VN) occurs within the martensite phase upon heating at 600 °C for 2 h.

Among the alloying elements in this martensite stainless steel, V is the strongest nitride-forming element, followed by Cr, Mo (minor amount), and Mn (minor amount) [52,53]. During formation of nitrides, there exists a competition among these elements. V atoms preferentially combine with N atoms to form nitrides, and the MN type is the most stable form for V-nitrides [54,55]. If V content is sufficient in the steel, almost all N atoms will form V-rich MN

type nitrides finally. In this V- and N-containing stainless steel, the amount of V atoms is not enough to form stable V-nitrides only, so the nearby Cr atoms also combine with N atoms to form Cr-nitrides, thereby Cr was also detected in the VN-rich region (Fig. 6). Cr₂N-rich (M₂N type) nitrides with a minor V content could form when V is insufficient in the steel [3], in agreement with our observation shown in Fig. 8.

In the tempering at high temperature, e.g. 600 °C, interstitial atoms (N) can diffuse much more readily than substitutional elements (Cr, V, Fe, etc.) [3,56]. Thus, in the martensite phase where V exists as solid solution, a slight aggregation of N atoms occurred (Fig. 7), resulting in V-rich VN as tempering nitrides (Fig. 8). Owing to the V enrichment in the tempering nitrides, no severe Cr consumption occurs, implying that the tempering process will not

cause the loss of passivity for the V- and N-containing martensite stainless steel austenitized at 1080 °C.

According to the Thermo-Calc calculation results shown in Supplementary Table 1, austenitization at both 1010 °C and 1080 °C resulted in the preferential dissolution of $M_{23}C_6$, which has lower thermal stability. The high N content restrained the precipitation of $M_{23}C_6$ and promoted the precipitation of M_2N simultaneously, which implies that the $M_{23}C_6$ induced Cr-depletion was alleviated, and the M_2N induced Cr-depletion was aggravated [19]. M_2N has a higher thermal stability than $M_{23}C_6$. Therefore, the relatively low austenitizing temperature (1010 °C) resulted in the insufficient dissolution of Cr_2N , leading to a lower Cr content in the matrix. The addition of N has been reported to contribute to the improvement of repassivation ability, because N can react with H^+ to form NH_3/NH_4^+ and thus alleviate acidification in pitting corrosion [18,57]. However, this positive effect no longer exists as the dissolved N in the matrix is saturated [19]. The excess N will consume the alloying elements that form the passive film, such as Cr. For the high-N tooling steel in this study, the formation of metal nitrides is necessary to achieve the required performance such as wear resistance and hardness. The best strategy for this martensite stainless steel with V and N is to allow V-nitrides to form primarily in the martensite since V is highly reactive with N. In addition to undissolved VN particles, excess N present in the form of solid solution may form Cr_2N , in a relatively small amount.

For the V- and N-containing martensitic stainless steel austenitized at 1010 °C, the dissolution of undissolved nitrides (Cr_2N) is insufficient inside the martensite phase, resulting in a lower Cr content in the matrix. The formation of tempering nitrides at 600 °C further consumes the alloying elements (especially Cr) in the martensite phase, which increases the inhomogeneity in the surface oxide film on the martensite phase (Fig. 9 and Supplementary Fig. 4), that is, the Cr_2O_3 content of the oxide film is lower in the areas where Cr content in the matrix is lower.

5. Conclusions

In this work, synchrotron-based hard X-ray photoelectron emission microscopy and spectroscopy (HAXPEEM and HAXPES) measurements were performed to investigate the chemical inhomogeneity of the native oxide film associated with the microstructure of a N- and V-containing martensitic stainless steel. Moreover, synchrotron-based microscopic X-ray absorption (μ -XAS) measurement utilizing a high brilliance and high flux soft X-ray beam, with in-situ heating, was performed to further reveal the nano-scale inhomogeneity and the evolution with increasing temperature from ambient temperature up to 600 °C relevant for tempering treatment. The fingerprinting features of the HAXPEEM and μ -XAS allowed for the high-resolution observation of the oxide film formed on various phases of the martensitic stainless steel as well as the composition difference caused by the formation of tempering nitrides. Based on the combined results, the following conclusions can be drawn:

(1) Synchrotron-based HAXPEEM/HAXPES in combination with μ -XAS measurements enabled, for the first time, analyses of thin oxide films formed on the micron- and nano-scale secondary phase particles in the martensitic matrix.

(2) The N- and V-containing martensitic stainless steel contain VN- and Cr_2N -type particles as secondary phase after austenitization process. The native oxide film on the Cr_2N particles is more enriched in Cr_2O_3 compared with that on the martensite matrix, on which a higher Fe oxide content is observed. The VN nitride domains contain trace amount of co-precipitated CrN particles, resulting an oxide film with a mixture of V oxides and Cr oxides.

(3) With the increase of temperature, the oxide growth rate on the martensite matrix is faster compared to that on the VN and

Cr_2N particles, due to the fast oxidation rate of metallic Cr in the martensite matrix and slow nitride-to-oxide transformation. The tempering at 600 °C promotes the formation of tempering nitrides (mainly VN particles) in the martensite matrix.

(4) The formation of VN-type tempering nitrides relieves the consumption of Cr from forming nitrides, which favours the formation of an oxide film with higher Cr_2O_3 content. The low austenitization temperature of 1010 °C strongly slows down the dissolution of VN and Cr_2N particles into the matrix, which results in reduced amounts of V and Cr in the martensite matrix and hence hampers the formation of an oxide film with higher contents of Cr_2O_3 and V oxides. The localised formation of tempering Cr nitrides within the martensite matrix further increases the inhomogeneity in the surface oxide film, giving rise to the risk for localized corrosion at the weak points of the oxide film (lower Cr_2O_3 content).

Declaration of competing interest

The authors declare that they have no known competing financial interests or personal relationships that could have appeared to influence the work reported in this paper.

CRediT authorship contribution statement

Xiaoqi Yue: Conceptualization, Data curation, Formal analysis, Investigation, Writing – original draft, Writing – review & editing. **Dihao Chen:** Data curation, Investigation, Writing – review & editing. **Anantha Krishnan:** Methodology, Writing – review & editing, Investigation, Resources. **Isac Lazar:** Formal analysis, Investigation, Software, Writing – review & editing. **Yuran Niu:** Data curation, Investigation, Methodology, Writing – review & editing. **Evangelos Golias:** Data curation, Writing – review & editing. **Carsten Wiemann:** Data curation, Formal analysis, Investigation, Methodology, Software, Writing – review & editing. **Andrei Gloskovskii:** Data curation, Investigation, Methodology, Writing – review & editing. **Christoph Schluter:** Methodology, Writing – review & editing. **Arno Jeromin:** Investigation. **Thomas F. Keller:** Investigation, Writing – review & editing. **Haijie Tong:** Investigation, Writing – review & editing. **Sebastian Ejnermark:** Resources. **Jinshan Pan:** Conceptualization, Investigation, Methodology, Writing – review & editing, Resources, Supervision.

Acknowledgements

This work was financially supported by the Vinnova (project number 2020-03778) and also partially supported by the [Swedish Research Council](#) (Vetenskapsrådet, project number 2021-04157). We acknowledge DESY for the beamtime on Beamline P22 at PETRA III under Proposal 20220855 and MAX IV Laboratory for the beamtime on Beamline MAXPEEM under Proposal 20221087. This research project has received funding from the EU's H2020 framework programme for research and innovation under grant agreement No 101007417 Nanoscience Foundries and Fine Analysis NFFA-Europe-Pilot for the access to the synchrotron radiation facility at the PETRA III beamline P22 and the DESY NanoLab under ID158. Research conducted at MAX IV, a Swedish national user facility, is supported by the [Swedish Research Council](#) under contract 2018-07152, the [Swedish Governmental Agency for Innovation Systems](#) under the contract 2018-04969, and Formas under contract 2019-02496.

Supplementary materials

Supplementary material associated with this article can be found, in the online version, at [doi:10.1016/j.jmst.2024.04.006](https://doi.org/10.1016/j.jmst.2024.04.006).

References

- [1] B. Gao, T. Xu, L. Wang, Y. Liu, J. Liu, Y. Zhang, Y. Sui, W. Sun, X. Chen, X. Li, L. Xiao, H. Zhou, *Corros. Sci.* 225 (2023) 111551.
- [2] Y. Zhao, W. Liu, Y. Fan, T. Zhang, B. Dong, L. Chen, Y. Wang, *Mater. Charact.* 175 (2021) 111066.
- [3] A.R. Gholi, G. Lindwall, M. Jönsson, Effects of tempering on corrosion properties of high nitrogen alloyed tooling steels in pyrolysis oil, Swerea KIMAB AB, The influence of pH and chloride concentration on the corrosion behaviour of AISI 316L steel in aqueous solutions, 2011. urn:nbn:se:kth:diva-40471.
- [4] P. Marcus, *Corros. Sci.* 36 (1994) 2155–2158.
- [5] S. Gao, H. Liu, X. Fang, W. Lu, S. Li, Y. Chen, S. Lu, *J. Electrochem. Soc.* 170 (2023) 021513.
- [6] M.-R. He, D.C. Johnson, G.S. Was, I.M. Robertson, *Acta Mater.* 138 (2017) 61–71.
- [7] A. Brooks, C. Clayton, K. Doss, Y. Lu, *J. Electrochem. Soc.* 133 (1986) 2459.
- [8] Y. Zhao, E. Zhou, Y. Liu, S. Liao, Z. Li, D. Xu, T. Zhang, T. Gu, *Corros. Sci.* 126 (2017) 142–151.
- [9] H. Amaya, T. Mori, K. Kondo, H. Hirata, M. Ueda, T. Mori, *CORROSION* 98, NACE International, Paper No. 98113, 1998.
- [10] E. De Vito, P. Marcus, *Surf. Interface Anal.* 19 (1992) 403–408.
- [11] X. Yue, Y. Ren, L. Huang, S. Zou, L. Zhang, Y. Hua, *Corros. Sci.* 194 (2022) 109935.
- [12] X. Yue, L. Zhang, Y. Wang, S. Xu, C. Wang, M. Lu, A. Neville, Y. Hua, *Corros. Sci.* 163 (2020) 108277.
- [13] X. Huang, D. Costa, B. Diawara, V. Maurice, P. Marcus, *Corros. Sci.* 224 (2023) 111543.
- [14] R. Willenbruch, C. Clayton, M. Oversluizen, D. Kim, Y. Lu, *Corros. Sci.* 31 (1990) 179–190.
- [15] Standard Test Methods for Pitting and Crevice Corrosion Resistance of Stainless Steels and Related Alloys by Use of Ferric Chloride Solution, (n.d.). <https://doi.org/10.1520/G0048-11R20E01>.
- [16] P. Marcus, M.E. Bussell, *Appl. Surf. Sci.* 59 (1992) 7–21.
- [17] J. Dai, H. Feng, H.-B. Li, Z.-H. Jiang, H. Li, S.-C. Zhang, P. Zhou, T. Zhang, *Corros. Sci.* 174 (2020) 108792.
- [18] X. Yue, Z. Yang, A. Larsson, H. Tang, S. Appelfeller, B. Sefer, A. Preobrajenski, J. Li, L. Zhang, J. Pan, *Npj Mater. Degrad.* 7 (2023) 79.
- [19] H. Feng, Z. Jiang, H. Li, P. Lu, S. Zhang, H. Zhu, B. Zhang, T. Zhang, D. Xu, Z. Chen, *Corros. Sci.* 144 (2018) 288–300.
- [20] Z. Jiang, H. Feng, H. Li, H. Zhu, S. Zhang, B. Zhang, Y. Han, T. Zhang, D. Xu, *Materials (Basel)* 10 (2017) 861.
- [21] M. Ras, P. Pistorius, *Corros. Sci.* 44 (2002) 2479–2490.
- [22] X. Yue, A. Larsson, H. Tang, A. Grespi, M. Scardamaglia, A. Shavorskiy, A. Krishnan, E. Lundgren, J. Pan, *Corros. Sci.* 214 (2023) 111018.
- [23] C. Örnek, F. Zhang, A. Larsson, M. Mansoor, G.S. Harlow, R. Kroll, F. Carlà, H. Hussain, D.L. Engelberg, B. Derin, *Appl. Surf. Sci.* 628 (2023) 157364.
- [24] G.S. Frankel, T. Li, J.R. Scully, *J. Electrochem. Soc.* 164 (2017) C180–C181.
- [25] A. Larsson, G. D'Acunto, M. Vorobyova, G. Abbondanza, U. Lienert, Z. Hegedüs, A. Preobrajenski, L.R. Merte, J. Eidhagen, A. Delblanc, *J. Alloy. Compd.* 895 (2022) 162657.
- [26] C.-O. Olsson, D. Landolt, *Electrochim. Acta* 48 (2003) 1093–1104.
- [27] A. Larsson, K. Simonov, J. Eidhagen, A. Grespi, X. Yue, H. Tang, A. Delblanc, M. Scardamaglia, A. Shavorskiy, J. Pan, E. Lundgren, *Appl. Surface Sci.* 611 (2022) 155714.
- [28] A. Barroux, T. Duguet, N. Ducommun, E. Nivet, J. Delgado, L. Laffont, C. Blanc, *Surf. Interfaces* 22 (2021) 100874.
- [29] G. Wei, S. Lu, S. Li, K. Yao, H. Luan, X. Fang, *Corros. Sci.* 177 (2020) 108951.
- [30] V. Marimuthu, I. Dulac, K. Kannoorpatti, *J. Bio-Tribo-Corrosion* 2 (2016) 17.
- [31] W.-C. Jiao, H.-B. Li, J. Dai, H. Feng, Z.-H. Jiang, T. Zhang, D.-K. Xu, H.-C. Zhu, S.-C. Zhang, *J. Mater. Sci. Technol.* 35 (2019) 2357–2364.
- [32] R. Fan, M. Gao, Y. Ma, X. Zha, X. Hao, K. Liu, *J. Mater. Sci. Technol.* 28 (2012) 1059–1066.
- [33] J. Yao, D.D. Macdonald, C. Dong, *Corros. Sci.* 146 (2019) 221–232.
- [34] M. Långberg, C. Örnek, F. Zhang, J. Cheng, M. Liu, E. Grånäs, C. Wiemann, A. Gloskovskii, Y. Matveyev, S. Kulkarni, *J. Electrochem. Soc.* 166 (2019) C3336.
- [35] A. Stierle, T.F. Keller, H. Noei, V. Vonk, R. Roehlsberger, Desy nanolab, *J. Large-Scale Res. Facilities* 2 (2016) A76.
- [36] C. Schlueter, A. Gloskovskii, K. Ederer, I. Schostak, S. Piec, I. Sarkar, Y. Matveyev, P. Lömkner, M. Sing, R. Claessen, C. Wiemann, C.M. Schneider, K. Medjanik, G. Schonhense, P. Amann, A. Nilsson, W. Drube, in: *AIP Conference Proceedings*, AIP Publishing, 2019.
- [37] Y. Niu, N. Vinogradov, A. Preobrajenski, C. Struzzi, B. Sarpi, L. Zhu, E. Golias, A. Zakharov, *J. Synchrotron Radiat.* 30 (2023) 468–478.
- [38] J. Schindelin, I. Arganda-Carreras, E. Frise, V. Kaynig, M. Longair, T. Pietzsch, S. Preibisch, C. Rueden, S. Saalfeld, B. Schmid, *Nat. Methods* 9 (2012) 676–682.
- [39] P. Thevenaz, U.E. Ruttimann, M. Unser, *IEEE Trans. Image Proc.* 7 (1998) 27–41.
- [40] J. Yao, D.D. Macdonald, C. Dong, *Corros. Sci.* 146 (2019) 221–232.
- [41] X. Yue, Z. Yang, L. Huang, L. Zhang, J. Li, Z. Xue, J. Pan, *J. Mater. Sci. Technol.* 127 (2022) 192–205.
- [42] A.S. Gomes, N. Yaghini, A. Martinelli, E. Ahlberg, *J. Raman Spectr.* 48 (2017) 1256–1263.
- [43] L. Zhu, A. Al-Sakeeri, F. Lenrick, O. Darselius Berg, P. Sjödin, A.A. Zakharov, A. Knutsson, A. Mikkelsen, *Surf. Interface Anal.* 54 (2022) 99–108.
- [44] M. Giménez-Marqués, E. Bellido, T. Berthelot, T. Simón-Yarza, T. Hidalgo, R. Simón-Vázquez, Á. González-Fernández, J. Avila, M.C. Asensio, R. Gref, *Small* 14 (2018) 1801900.
- [45] E. Yitamben, T. Lovejoy, A. Pakhomov, S. Heald, E. Negusse, D. Arena, F. Ohuchi, M. Olmstead, *Phys. Rev. B* 83 (2011) 045203.
- [46] S. Kalal, S. Nayak, S. Sahoo, R. Joshi, R.J. Choudhary, R. Rawat, M. Gupta, *Sci. Rep.* 13 (2023) 15994.
- [47] R. Kapoor, S. Oyama, B. Frühberger, J. Chen, *J. Phys. Chem. B* 101 (1997) 1543–1547.
- [48] K. Robert, D. Stiévenard, D. Deresmes, C. Douard, A. Iadecola, D. Troadec, P. Simon, N. Nuns, M. Marinova, M. Huvé, *Energy Environ. Sci.* 13 (2020) 949–957.
- [49] D. Maganas, M. Roemelt, M. Hävecker, A. Trunschke, A. Knop-Gericke, R. Schlögl, F. Neese, *Phys. Chem. Chem. Phys.* 15 (2013) 7260–7276.
- [50] N. Pandey, M. Gupta, D. Phase, A. Gupta, *J. Synchrotr. Radiation* 28 (2021) 1504–1510.
- [51] T.C. Rojas, A. Caro, G. Lozano, J. Sánchez-López, *Solar Energy Mater. Solar Cells* 223 (2021) 110951.
- [52] X.-S. Guan, Y. Nishizawa, K. Okamura, H. Numakura, M. Koiwa, *Mater. Sci. Eng. A* 370 (2004) 73–77.
- [53] S.-W. Young, M. Sato, K. Yamamitsu, Y. Shimada, Y. Zhang, G. Miyamoto, T. Furuhara, *Acta Mater.* 206 (2021) 116612.
- [54] H. Lee, J. Kong, D. Lee, H. On, J. Sung, *Mater. Des.* 30 (2009) 1691–1696.
- [55] Y.Z. Shen, S.H. Kim, H.D. Cho, C.H. Han, W.S. Ryu, *J. Nucl. Mater.* 400 (2010) 94–102.
- [56] A. Goecmen, R. Steins, C. Solenthaler, P.J. Uggowitzer, M.O. Speidel, *ISIJ Int.* 36 (1996) 768–776.
- [57] R. Jargelius-Pettersson, *Corros. Sci.* 41 (1999) 1639–1664.